2017-3905

AIAA Aviation and Aeronautics Forum and Exposition, 59 June 2017, Denver, Colorado

Efficient Evaluation of Dynamic Response Data with a Linearized Frequency Domain Solver at Transonic Separated Flow Conditions

Markus Widhalm* and Reik Thormann†

Deutsches Zentrum für Luft und Raumfahrt (DLR), Braunschweig, 38108, Germany

Deutsches Zentrum für Luft und Raumfahrt (DLR), Göttingen, 37073, Germany

Each perturbation of an aircraft state in trim induces aerodynamic loads on wings, control surfaces and other parts of an aircraft. These loads have to be quantified for a wide range of flight states covering the flight envelope. Small disturbance approaches based on the Reynolds-averaged Navier Stokes equations fulfil the requirements of efficiently predicting accurate dynamic response data. These time-linearized methods have been successfully applied in flight dynamic and aeroelastic analyses for moderate flight conditions. Small disturbance approaches on the basis of Navier-Stokes solvers have become most often the right choice, for example in flight dynamic and aeroelastic analysis, to combine efficiency and accuracy for predicting dynamic response data. However, in complex flows exhibiting shock-induced separations, deficits in robustness of the iterative solution methods often lead to simplifications of the equations and thus reducing the quality of the computed results. The presented linearized frequency domain solver has shown accurate results compared to nonlinear time-accurate unsteady simulations for attached flow conditions. The area of application is extended to separated transonic flows demonstrating the method's capability to accurately capture strong shock-boundary interactions. Deriving the exact linearization of the turbulence model as well as implementing a robust method to solve the stiff linear systems are key tasks to achieve this target. Results are presented for the LANN wing undergoing rigid body motions comparing dynamic derivatives of lift and moment coefficients between the linearized frequency domain solver and its time-domain counterpart. In addition, local surface pressure and skin friction coefficients are analysed at two span stations. The presented linearized frequency domain solver (TAU-LFD) has shown accurate results in comparison to fully time-accurate unsteady simulations at separated transonic flow conditions.

Nomenclature

Variables

f	frequency, Hz
$\mathbf{n}$	face normal vector with components n_x, n_y and n_z
$\|\Omega\|$	dual grid control-volume
t	physical time, s
c_p	pressure distribution coefficient
c_f	skin friction coefficient
C_L	lift coefficient
C_m	pitching moment coefficient
Re	real part
Im	imaginary part

*Research Engineer, Institute of Aerodynamics and Flow Technology, CASE branch, email:markus.widhalm@dlr.de.

†Research Engineer, Institute of Aeroelasticity, Aeroelastic Simulation Depart., Member AIAA. Currently at Univeristy of Liverpool

2017

Superscripts

$\bar{}$ time-invariant mean state
$\hat{}$ Fourier coefficient, perturbation amplitude
$\dot{}$ temporal derivative, $\partial/\partial t$

I. Introduction

The analysis of the flight dynamic characteristic of an aircraft is important for the prediction of satisfactory performance and control behavior. Considering an initial aircraft situation in a trimmed steady flight condition, as the aircraft proceed on a flight path, changes and oscillations occur in airspeed, altitude and angle of attack. Dynamic response data are measures how the aerodynamic forces and moments on an aircraft change as these flight attitude parameters change. Thus, dynamic response data are an essential part to determine the aircraft flight characteristic from which the limits of the stability region of an aircraft follows. The type and strength of an aircraft movement may depend on the broad utilization range which most often result in a nonlinear behavior of the encountered air loads. The complexity of flight attitudes can be reduced under certain circumstances and assumptions to describe successfully the motion behavior of aircraft in the linear region. The calculation of stability bounds of aircraft is mainly conducted with a small disturbance approach of the rotational and the translational rigid body equations of motion, formulated initially by Bryan[1] and summarized by Etkin.[2] The essential prerequisite of this reduced order method is based on the assumption that the considered system of equations behave dynamically linear and is linear time-invariant.

Regarding flight dynamic analysis, the deduced system are linear, ordinary, second-order differential equations in time with constant coefficients. The linearized equations of motion reflects the global aerodynamic forces and moments which are introduced via a Taylor series expansion, neglecting higher order terms. The coefficients in the differential equations describe the mass, inertia characteristics and the aerodynamic stability derivatives of the aircraft. The differential equations can be solved in the time domain or in the frequency domain. Usually the latter is preferred because it reduces considerably algebraic manipulation. On the other hand, aeroelastic analysis refers to the discrete solution of the dynamic response on the surface as structural modes need to be resolved.

Over decades, wind tunnel experiments were the backbone to establish confidence on dynamic derivatives on the basis of forced motions.[3–5] Since these are unsteady motions, the numerical simulation process with time-accurate CFD techniques is time consuming, presuming a satisfactory prediction quality. Unsteady Reynolds-averaged Navier-Stokes (URANS) methods provide accurate predictions in transonic and separated flow regions. Despite enormous progress in efficient solution techniques, URANS simulations are still expensive and time consuming if applied for aerodynamic loads prediction of aircraft. Hence, the application area is most often limited to a small range of parameters in the flight envelope. Numerical methods based on the linear potential theory, e.g. Doublet-Lattice Methods (DLM), have made a respectable contribution on estimating dynamic derivatives of aerodynamic forces and moments. Regarding numerical efficiency, the low fidelity DLM-simulations are unsurpassed. Linear, thin-airfoil, potential flow theory starts to lose its validity when approaching the transonic region and is therefore not able to give satisfactory approximations to aerodynamic forces and moments. There are several empirical methods used to correct the representation of the aerodynamic forces in this region. A common method uses experimental steady and quasi-steady aerodynamic force data. Using a relatively straightforward approach, a correction factor based on the steady-state lift curve slope is applied to all unsteady aerodynamic force data. Specifically, this correction factor is obtained by calculating, at each Mach number, the ratio of experimental-to-analytical lift curve slope for the vehicle. That ratio is most often mispredicted because of missing frequency and damping characteristics as investigated by Newsom and Pototzky.[6] Also DLM are extended with corrections for the transonic regime based on wind-tunnel tests to improve the prediction quality to a certain confidence.[7] The general applicability is often not guaranteed as the aircraft aerodynamic behavior grow in complexity which results in time-consuming testing.

In terms of numerical methods, assuming small perturbations of the flight parameters may reduce the

complexity and linear behavior can be expected again. The approach deals with a trimmed aircraft under a set of steady flight conditions related to constant altitude, angle of attack, airspeed and controls. The analysis is then applied to a range of flight parameters considering only small oscillations about the trimmed steady flight condition. That is, applying a truncated discrete Fourier series to model a certain amount of harmonic excitations by solving a linear system of equation. Linearized methods on the basis of RANS solvers have impacted that field significantly. The underlying assumption is a periodical motion combined with small excitations of flight parameters.

These technique models unsteadiness as a small-amplitude perturbation linearized at a nonlinear steady-state background flow and solves the equations for only one harmonic at a time. Hence, they remain the RANS methods high-fidelity behavior to a certain degree with a remarkable reduction in computational costs. Approaches for predicting unsteady viscous flows date back to Clark and Hall[8] to determine the onset of stall flutter. The initial work of the presented linearized frequency domain (LFD) approach implemented in the DLR TAU-Code relates to works of Clark and Hall[8] and McMullen et.al.[9] for the Navier-Stokes equations.

Alternative contributions for computing stability derivatives are made by Limache and Cliff.[10] They showed that the estimation of stability derivatives by applying a sensitivity approach based on a single steady-state flow simulation gains accurate results. A remarkable side effect is the straight forward determination of the split stability derivative, static or dynamic, which may be favorable for certain applications. Regarding forced-oscillation approaches, the combined derivative is obtained. It follows naturally using automatic differentiation to compute derivatives from sensitivities which is accomplished by Park et.al.[11] and used successfully in an optimization framework by Mader and Martin.[12]

Since this work is the basis for flight dynamic stability analysis and aeroelastic applications, the LFD has been preferred. Subsonic and transonic attached flows are resolved reasonably well with these approaches for three-dimensional applications as shown by Widhalm et. al.,[13] Mialon[14] and Pechloff and Laschka.[15] However, the frozen-turbulent eddy-viscosity approach is a common choice for many applications due to robustness issues encountered in the numerical solution process (Dufour[16]). According to developments by Chassiang,[17] Pechloff and Laschka[18] used a limiting procedure for the turbulent transport variable as a stabilizing technique for the pseudo-time marching method and obtained good results for the NASA clipped delta wing with strong shocks. In conjunction with strong leading edge vortices that approach show relatively large deviations in comparison to URANS simulations. In a RANS framework, the linearization of turbulent stresses may become important at strong-shocks as found by Kim et. al.[19] using various two-equation turbulence models for his survey. In addition, if separation appears the linearization of the turbulent stresses become evident for accurate results, as reported by Thormann and Widhalm[20] for the NACA64 A010 profile in viscous transonic and separated flow conditions. Notably, it has been favored to fully account for the eddy viscosity's perturbation amplitude within the small disturbance Navier-Stokes equations, as supplied by an accordant formulation of the Spalart-Allmaras (S-A) turbulence transport-equation and auxiliary functions.

Instead of using a pseudo-time marching iterative procedure for solving the linear system of equations which may cause numerical instabilities, a preconditioned Krylov-GMRES[21] solution scheme was implemented in this work. This method achieves a remarkable efficiency and its stabilizing effect has been demonstrated by Campobasso and Giles[22] for turbo-machinery aeroelasticity. The LFD together with the pre-conditioning method, proposed by McCracken,[23] is implemented in the TAU-Code.

The overall good prediction quality and satisfactory CPU-time reduction factor for the LFD RANS method were presented by the authors for the LANN wing (CT5 case) in the transonic attached flow regime. Investigations are performed with rigid pitch and plunge oscillations for strong-shock and detached flow conditions with the high-aspect-ratio LANN wing[24] (CT9 case). Derivatives of the lift and pitching moment coefficient as well as surface pressure and skin friction coefficient distributions are compared to their URANS counterparts for several reduced frequencies. Observed time reduction factors between LFD and URANS are reported for emphasizing the LFD's efficiency gain.

II. Linearized frequency domain method

The considered governing equations are the mass-weighted (Favre) averaged three-dimensional instantaneous Navier-Stokes equations, with the Spalart-Allmaras (S-A) one equation turbulence model[25] providing eddy viscosity closure. Discretized in space with a finite volume method and assuming rigid body motions,

the URANS equation can be written in semi-discrete form as

$$\frac{\mathrm{d}\mathbf{M}\mathbf{W}}{\mathrm{d}t} + \mathbf{R}(\mathbf{W}, \mathbf{x}, \dot{\mathbf{x}}) = 0, \tag{1}$$

where $\mathbf{R}$ denotes the nonlinear residual corresponding to the state vector of conservative variables $\mathbf{W} := \mathbf{W}(\mathbf{x}, \dot{\mathbf{x}})$. In Eq. (1) $\mathbf{x} := \mathbf{x}(t)$ are the time-dependent grid-node coordinates, and $\dot{\mathbf{x}} := \dot{\mathbf{x}}(\mathbf{x}(t))$ denotes the grid-node velocities. The mass matrix is described as $\mathbf{M} := \mathbf{M}(\mathbf{x}) = \mathrm{diag}\,|\Omega_i(t)|$ with dimension of total number of control-volumes. The grid deformation represented by $\mathbf{x}$ is prescribed, and thus Eq. (1) can be solved for $\mathbf{W}$.

Postulating the considered body's time-dependent deflection to be of small amplitude, the flow response to the excitation can be considered to be predominately dynamically linear. Thus, higher order time-dependencies in the flow response can be neglected, allowing it to be separated into a time-invariant mean state and a time-dependent small perturbation. On this basis, $\mathbf{W}$ can be linearized about an individual grid node's steady-state location using a Taylor-series expansion, that terminates after the first-order term:

$$\begin{aligned}
\mathbf{W}(\mathbf{x}) &\approx \overline{\mathbf{W}} + \frac{\partial \mathbf{W}}{\partial \mathbf{x}}(\mathbf{x} - \bar{\mathbf{x}}), \\
\mathbf{x}(t) &\approx \bar{\mathbf{x}} + \frac{\partial \mathbf{x}}{\partial t}(t - \bar{t}), \quad \dot{\mathbf{x}}(t) = \frac{\mathrm{d}\mathbf{x}}{\mathrm{d}t}, \quad \dot{\bar{\mathbf{x}}} \equiv 0, \\
\mathbf{M}(\mathbf{x}) &\approx \overline{\mathbf{M}} + \frac{\partial \mathbf{M}}{\partial \mathbf{x}}(\mathbf{x} - \bar{\mathbf{x}}), \\
\mathbf{R}(\mathbf{W}, \mathbf{x}, \dot{\mathbf{x}}) &\approx \overline{\mathbf{R}}(\overline{\mathbf{W}}, \bar{\mathbf{x}}, \dot{\bar{\mathbf{x}}}) + \widetilde{\mathbf{R}}(\overline{\mathbf{W}}, \bar{\mathbf{x}}, \dot{\bar{\mathbf{x}}}, \widetilde{\mathbf{W}}, \tilde{\mathbf{x}}, \dot{\tilde{\mathbf{x}}}).
\end{aligned} \tag{2}$$

Moreover, expressing the perturbations in terms of a Fourier series and considering merely a first harmonic excitation and response ($n_h = 1$)

$$\begin{aligned}
\mathbf{W} - \overline{\mathbf{W}} &:= \mathcal{R} \sum_{n_h=1}^{\infty} \widehat{\mathbf{W}}_{n_h} e^{i n_h \omega t} \approx \widehat{\mathbf{W}} e^{i\omega t}, \;\; \widehat{\mathbf{W}}_{n_h} \in \mathbb{C} \\
\mathbf{x} - \bar{\mathbf{x}} &:= \mathcal{R} \sum_{n_h=1}^{\infty} \hat{\mathbf{x}}_{n_h} e^{i n_h \omega t} \approx \hat{\mathbf{x}} e^{i\omega t}, \dot{\mathbf{x}} \approx \hat{\mathbf{x}} i\omega e^{i\omega t}, \;\; \hat{\mathbf{x}}_{n_h} \in \mathbb{R}
\end{aligned} \tag{3}$$

where ω denotes the base angular velocity in rad/s ($\omega = 2\pi f$). Equation (1) can be transformed into the frequency domain. Applying Eq. (2) to Eq. (1) by neglecting higher order terms yields a separate linear system of equations linearized at steady-state conditions $(\overline{\mathbf{W}}, \bar{\mathbf{x}}, \dot{\bar{\mathbf{x}}})$ for one harmonic excitation. Thus, Eq. (1) becomes

$$\left[i\omega\, \overline{\mathbf{M}} + \frac{\partial \mathbf{R}}{\partial \mathbf{W}} \right] \widehat{\mathbf{W}} = - \left[\frac{\partial \mathbf{R}}{\partial \mathbf{x}} + i\omega \left(\frac{\partial \mathbf{R}}{\partial \dot{\mathbf{x}}} + \overline{\mathbf{W}} \frac{\partial \mathbf{M}}{\partial \mathbf{x}} \right) \right] \hat{\mathbf{x}}. \tag{4}$$

The physical validity of the result will depend on the degree to which the assumption of small perturbations is satisfied, and thus to the degree of dynamic nonlinearity in the actual flow response. Ultimately, the nonlinear governing equations system has been reduced to a complex linear system of equations for the amplitude state vector.

II.A. Jacobians of the linear system

The flow residual $\mathbf{R}$ (Eq. (1)) depends on the flow variables, grid-node coordinates and grid-node velocities. Derivatives of the discrete residual for those dependencies are required to build the linear system for the LFD. One of the most important procedures for the preparation of analytically derived derivatives is the consequent application of the chain rule. Hence, the total derivative of $\mathbf{R}$ with respect to $\mathbf{W}$, $\mathbf{x}$ and $\dot{\mathbf{x}}$ is

$$\mathbf{R} := \mathbf{R}(\mathbf{W}, \mathbf{x}, \mathbf{n}(\mathbf{x}), |\Omega|(\mathbf{x}, \mathbf{n}(\mathbf{x})), \dot{\mathbf{x}}), \tag{5}$$

$$\frac{\mathrm{d}\mathbf{R}}{\mathrm{d}\mathbf{W}} = \frac{\partial \mathbf{R}}{\partial \mathbf{W}}, \quad \frac{\mathrm{d}\mathbf{R}}{\mathrm{d}\mathbf{x}} = \frac{\partial \mathbf{R}}{\partial \mathbf{x}} + \frac{\partial \mathbf{R}}{\partial \mathbf{n}} \frac{\partial \mathbf{n}}{\partial \mathbf{x}} + \frac{\partial \mathbf{R}}{\partial |\Omega|} \left(\frac{\partial |\Omega|}{\partial \mathbf{n}} \frac{\partial \mathbf{n}}{\partial \mathbf{x}} + \frac{\partial |\Omega|}{\partial \mathbf{x}} \right), \quad \frac{\mathrm{d}\mathbf{R}}{\mathrm{d}\dot{\mathbf{x}}} = \frac{\partial \mathbf{R}}{\partial \dot{\mathbf{x}}}, \tag{6}$$

where $\mathrm{d}\mathbf{R}/\mathrm{d}\mathbf{W}$ is the flux Jacobian, which has been derived in a previous work by Dwight[26] for the main equations. The S-A turbulence model linearization has been added accordingly to account for a consistent

and accurate derivation of the LFD method. $\mathrm{d}\mathbf{R}/\mathrm{d}\mathbf{x}$ is the grid Jacobian. Grid-node velocity derivatives are derivatives which appear for a moving coordinate frame and are evaluated entirely from the discrete residual equation.

Regarding the structure of derivatives, Eq. (6), $\mathbf{R}$ is a vector of dimension, $n \times N$, where n is the number of grid nodes, and N belongs to the equations to be solved per node. The flow variables $\mathbf{W}$ have the same dimension $n \times N$, while grid node and grid node velocities are vectors of dimension $n \times 3$. Hence, matrices arise with size of $(n \times N) \times (n \times N)$ for $\mathrm{d}\mathbf{R}/\mathrm{d}\mathbf{W}$, and size of $(n \times N) \times (n \times 3)$ for $\mathrm{d}\mathbf{R}/\mathrm{d}\mathbf{x}$ as well as $\mathrm{d}\mathbf{R}/\mathrm{d}\dot{\mathbf{x}}$. These matrices can be reordered to obtain block-wise structures of the form $(n \times n)$ with blocks of $N \times N$ or $N \times 3$. The notation for block-wise differentiation, for example $\mathrm{d}\mathbf{R}_i/\mathrm{d}\mathbf{x}_j$, corresponds to the derivative of the i-th component of $\mathbf{R}$ with respect to the j-th component of $\mathbf{x}$.

An important note about the components of these matrices is their sparse fill-in because $\mathbf{R}$ at node i is often dependent on next neighbors of i only. Convenient storage approaches are an important part of these linear systems. However, derivatives of $\mathbf{R}$ may be multiplied with a vector instantly to reduce the size of the matrix to a practical dimension of $n \times N$ or $n \times 3$.

Regarding Eq. (6), the evaluation of derivatives can be split, into the following components:

$$\frac{\mathrm{d}\mathbf{R}}{\mathrm{d}\mathbf{W}}, \quad \frac{\partial \mathbf{R}}{\partial \mathbf{x}}, \quad \frac{\partial \mathbf{R}}{\partial \mathbf{n}}, \quad \frac{\partial \mathbf{R}}{\partial |\Omega|}, \quad \frac{\mathrm{d}\mathbf{R}}{\mathrm{d}\dot{\mathbf{x}}}, \tag{7}$$

which are constructed from residual (flow solver) routines, while derivatives

$$\frac{\partial \mathbf{n}}{\partial \mathbf{x}}, \quad \left(\frac{\partial |\Omega|}{\partial \mathbf{n}} \frac{\partial \mathbf{n}}{\partial \mathbf{x}} + \frac{\partial |\Omega|}{\partial \mathbf{x}} \right), \tag{8}$$

are related to dual grid routines only. That independence of flow solver and dual grid metric routines allows for consecutive building of derivatives.

II.A.1. Rigid body motion description

One missing term in Eq. (4) still needs to be arranged: $\hat{\mathbf{x}}$. $\hat{\mathbf{x}}$ is a derivative again, similar to a derivative of the form $\partial \mathbf{x}/\partial \alpha$, where α denotes a rigid body motion. Hence, $\hat{\mathbf{x}}$ describes the dependence of the grid nodes in relation to a prescribed motion.

Denoting $\boldsymbol{\varphi} = [\phi, \theta, \psi]^T$ as the vector of three independent rotation angles, the simplest form of the motion of a grid node undergoing a pure rigid body motion around the center of rotation is defined as

$$\begin{aligned} \mathbf{x}(\mathbf{x}_t, \boldsymbol{\varphi}) &= (\mathbf{T}_{gb}(\boldsymbol{\varphi})\mathbf{x}_b - \mathbf{x}_b) + \mathbf{x}_{b,t}, \quad \mathbf{x}_b = \mathbf{x}^0 - \mathbf{x}_r^0, \\ \frac{\partial \mathbf{x}}{\partial \alpha} &= \frac{\partial \mathbf{T}_{gb}(\boldsymbol{\varphi})}{\partial \alpha}\mathbf{x}_b + \frac{\partial \mathbf{x}_t}{\partial \alpha}, \end{aligned} \tag{9}$$

where $\mathbf{x}_{b,t}$ denotes the translation vector and subscript b is related to the body-fixed frame of reference. The rotation matrix is defined as

$$\mathbf{T}_{gb}(\boldsymbol{\varphi}) = \begin{bmatrix} \cos\theta\cos\psi & \sin\phi\sin\theta\cos\psi - \cos\phi\sin\psi & \cos\phi\sin\theta\cos\psi + \sin\phi\sin\psi \\ \cos\theta\sin\psi & \sin\phi\sin\theta\sin\psi + \cos\phi\cos\psi & \cos\phi\sin\theta\sin\psi - \sin\phi\cos\psi \\ -\sin\theta & \sin\phi\cos\theta & \cos\phi\cos\theta \end{bmatrix}, \tag{10}$$

which describes the shift from the body-fixed into the geodesic frame of reference. In Eq. (9), $\mathbf{x}(\mathbf{x}_t, \boldsymbol{\varphi})$ is the unknown volume node displacement, and $\mathbf{x}_b$ the known description of the surface mesh node, which have been taken to be functions of $\alpha \in [\mathbf{x}_{b,t}, \boldsymbol{\varphi}]$ which summarizes the six degree of freedom motion.

II.B. Solution method

A critical part is to solve the large linear system (4) with the dimension $n_p \times n_{\mathrm{eq}} \times 2$, where n_p denotes the number of grid nodes, n_{eq} the number of flow equations and 2 represents the real and imaginary part. In particular for separated flows and small reduced frequencies, experience has shown that the linear system often becomes ill-conditioned and the iterative procedure may stall or diverge. Applying an efficient

preconditioner may increase the robustness of the method substantially. Thus, the LFD employs an ILU preconditioner based on a modified first and second order accurate flux Jacobian following the approach in:[23]

$$\left(\frac{\partial \mathbf{R}}{\partial \mathbf{W}}\right)^{\text{pre}} = \xi \frac{\partial \mathbf{R}^{\text{2nd}}}{\partial \mathbf{W}} + (1-\xi)\frac{\partial \mathbf{R}^{\text{1st}}}{\partial \mathbf{W}}, \quad \xi \in [0,1], \tag{11}$$

where $\mathbf{R}^{\text{1st}}$ is the first order spatial residual and $\mathbf{R}^{\text{2nd}}$ is the second order spatial residual, respectively. The corresponding flux Jacobians have different sparsity patterns as well, because a larger stencil is necessary for a second order than for a first order residual. Naturally, the convergence rate of the LFD solver is dependent on the weighting factor, and a suitable factor was found to be $\xi = 0.5$.[27]

The approximation is used for the preconditioner to improve robustness. The solver for the linear system is a restarted GMRES subspace solver[28] based on a second order accurate residual. In parallel simulations, the preconditioner is applied on each sub domain independently to reduce time consuming MPI communications. Beforehand, the implementation was realized by doubling the dimension of the preconditioning matrix to solve the real and imaginary part separated. Computational more efficient in terms of memory consumption is the complex ILU preconditioner applied to the solution of the complex harmonic equations.

Evaluation of the pressure $\hat{c}_p$ and skin friction coefficient $\hat{c}_f$: After receiving the solution state vector in conservative formulation it will be transformed into a primitive state vector to calculate real and imaginary pressure and skin friction coefficient distributions on the surface grid nodes. Quantities of interest are computed from $\widehat{\mathbf{W}}$ such as

$$c_p = \frac{p_{\text{wall}} - p_\infty}{\frac{1}{2}\rho_\infty U_\infty^2}, \quad \hat{c}_p := \hat{c}_p(\bar{p}, \hat{p}) = \frac{2\hat{p}}{\rho_\infty u_\infty^2}, \quad \hat{p} = \frac{\partial p}{\partial \mathbf{W}}\widehat{\mathbf{W}}, \tag{12}$$

and p_{wall} denotes the pressure at the wall. Freestream values ρ_∞, U_∞ and p_∞ are density, velocity and pressure, respectively. The surface skin friction coefficient evaluation is based on the formula:

$$\mathbf{c}_f = \frac{\boldsymbol{\tau}\mathbf{n}}{\frac{1}{2}\rho_\infty U_\infty^2}, \quad c_{f_x} = \text{sgn}(u_{n_p})\|\mathbf{c}_f\|. \tag{13}$$

where $\boldsymbol{\tau}$ denotes the shear-stress tensor. The coefficient is multiplied with the sign of the first component of the velocity vector, $\text{sgn}(u_{n_p})$, which is the next neighboring node perpendicular to the viscous wall. $\hat{c}_{f_x}$ on a viscous wall is obtained by differentiation with the chain rule

$$\hat{c}_{f_x} = \frac{\partial c_{f_x}}{\partial \mathbf{W}}\widehat{\mathbf{W}} = \text{sgn}(u_{n_p})\frac{2}{\rho_\infty U_\infty^2}\left(\frac{\partial \mu_{\text{eff}}}{\partial \mathbf{W}}\|\mathbf{S}\| + \mu_{\text{eff}}\frac{\partial \|\mathbf{S}\|}{\partial \mathbf{W}}\right)\widehat{\mathbf{W}}. \tag{14}$$

The detailed derivation of $\hat{c}_{f_x}$ is found in the appendix.

III. Results for the LANN Wing - CT9 case

The AGARD LANN wing,[24] fig. 1(a), is a trapezoidal high-aspect-ratio wing, representative of transport aircraft flying at transonic speeds. It has a taper ratio of 0.4 and an aspect ratio of 7.92. The ratio between the semi span and root chord length is about 2.77 with a mean aerodynamic chord length ($l_{ref} = c_{AC}$) of 0.268 m, The flow conditions are at a freestream Mach number of $\text{M}_\infty = 0.82$, a Reynolds number of $\text{Re}_\infty = 7.3 \times 10^6$, and a mean angle of attack of $\bar{\alpha} = 2.6\,\text{deg}$.

The structured computational grid around the LANN wing with a blunt trailing edge, fig. 1(a), consists of about 1.15 million grid nodes. The location of the pitching axis as well as the location of span stations are outlined in fig. 1(a) for comparison of URANS and LFD surface pressure and skin friction coefficient distributions. The farfield distance is set to ten root chord lengths and the distances of the first off-body grid nodes all satisfy $y^+ < 0.5$ in sublayer scale. The wing performs a forced sinusoidal pitching motion about an axis parallel to the y-axis (with $x_\text{r} = 0.62$), as governed by

$$\alpha(\tau) = \bar{\alpha} + \hat{\alpha}\cdot\sin(k\,\tau) = \bar{\alpha} + \tilde{\alpha}(\tau), \quad \tau = \frac{U_\infty t}{l_{ref}}, \tag{15}$$

with the reduced frequency

$$k = \frac{\omega\, l_{ref}}{U_\infty}, \quad \omega = 2\pi f, \tag{16}$$

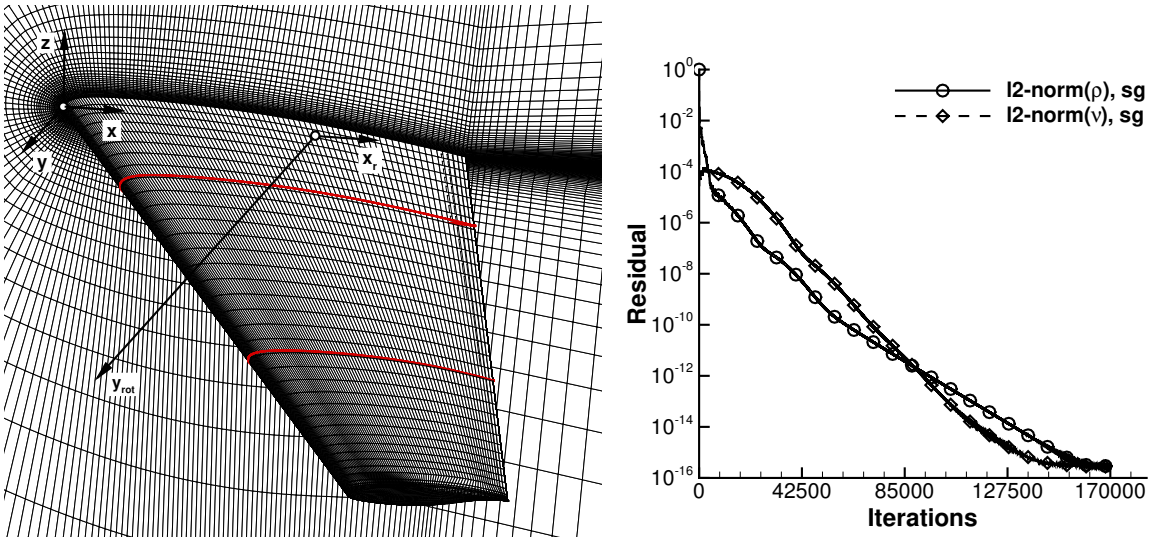

(a) AGARD LANN wing

(b) Steady-state convergence

Figure 1. (a) Computational surface grid resolution for the AGARD LANN wing (b) indicating the location of the pitch axis (y) and both planes, y/s=0.2 as well as y/s=0.65, for extracting surface pressure and skin friction coefficients. (b) Convergence history of the steady-state flow simulation for the density (ρ) and S-A working variable ($\tilde{\nu}$) residual (b) for the CT9 case (sg - single grid).

where U_∞ is the freestream velocity.

Figure 1(b) presents the steady-state convergence history to machine accuracy, about fifteen orders of magnitude, for the density, and S-A working variable residual. Applying multi-gridding for that case caused a stalling of the residual before reaching machine accuracy, thus, this case was performed with single grid (sg), increasing the steady-state simulation time considerably. This solution of the steady-state simulation with the residual of $\mathbf{R} \approx 0$, facilitates to be a suitable initial solution for the unsteady dual-time stepping scheme and simultaneously fulfills the condition for the LFD method.

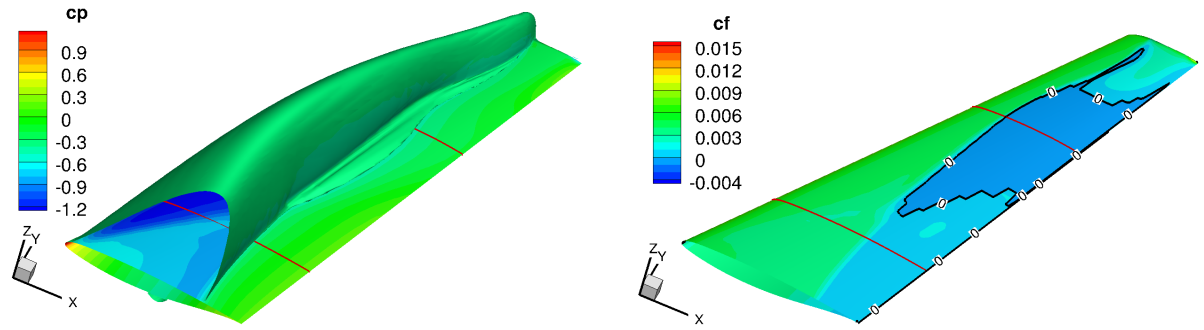

(a) c_p, sonic boom

(b) c_f

Figure 2. (a) Surface pressure coefficient distribution and sonic boom marking the strong shock system for the steady-state flow simulation, ($M_\infty = 0.82$, $Re_\infty = 7.3 \times 10^6$, $\bar{\alpha} = 2.6$ deg.) and (b) surface skin friction distribution showing the shock induced separation zone enclosed in the $c_f \equiv 0$ line.

Figure 2 visualize the steady-state surface pressure and skin friction coefficient as well as the location of the sonic boom. The steady-state flow simulation for the wing exhibits a strong λ-type shock system on the upper surface as shown with the $M_\infty = 1$ isosurface in fig. 2(a). The shock ends at the mid-wing nearly perpendicular to the surface, and it is located upstream from the leading edge and extends downstream to mid-wing approximately, as measured from the root to the wing tip. A weaker shock occurs on the lower surface at the root of the wing. The lower surface shock system extends to the wing tip. Figure 2(b) indicates the separation zone on the upper surface enclosed in the surface skin friction contour line of $c_f \equiv 0$. The massive shock induced separation at the mid-wing extends downstream to the trailing edge and can be considered important for the general applicability of the LFD method.

Table 1. Computational parameters employed in the LFD and URANS simulation of the CT9 case.

Parameter	Values
LFD	
minimum residual abort criterion	1×10^{-8}
Krylov-GMRES iterations	60-210
ILU 2^{nd} order preconditioning weight, ξ	0.5-0.6
CFL number (fine)	10/-
URANS	
physical time-steps/period	350
maximum pseudo time iterations	1000
multigrid cycle	single grid
minimum residual abort criterion (absolute)	1×10^{-7}
Number of periods	4-6
CFL number (fine/coarse)	10/-

Simulation parameters for URANS and LFD method are listed in table 1. Time steps per period has been set to 350 because of missing multigrid and periods range between 4 ($k < 0.4$), 5 periods for $k = 0.4$ to 0.8 and 6 periods for the $k = 1.0$ instance. Restart vectors for the GMRES method for case CT9 had to be risen more than three times the initial setting of sixty for $k <= 0.4$ up to 210 restart vectors at $k = 1$ to assure convergence.

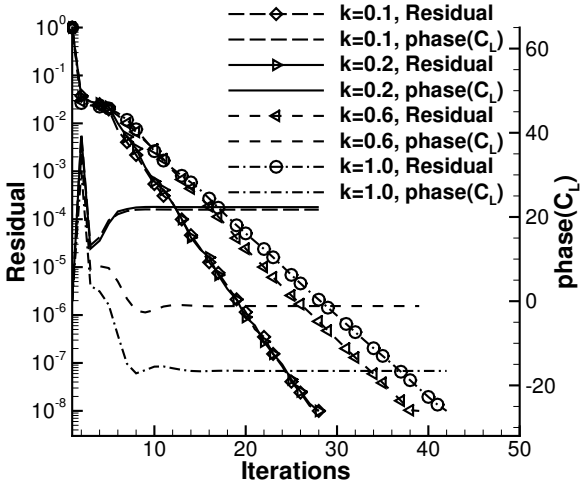

Figure 3. LANN CT9 baseline case comparison of the residual and phase shift of C_L history of the LFD method for various k cases, when using the GMRES-ILU preconditioning scheme.

Figure 3 shows the convergence behavior of the LFD method for selective k cases. The l_2-norm residual, normalized with the residual of the first cycle, reached 1×10^{-8} for all simulations. The convergence behavior of the LFD method is independent for moderate k values ($k <= 0.2$), since robust solution techniques as Krylov-GMRES[28] (GMRES) with incomplete LU (ILU)[21,23] preconditioning are employed. Too less restart vectors often indicate an alternating stalling and convergence at the beginning of the simulation with a complete stall after a certain order of residual drop. To overcome this behavior the restart vectors are gradually increased until convergence could be ascertained. Regarding the ILU-preconditioner, the weighting factor ξ has been slightly increased from 0.5 to 0.6 but improves marginally the robustness for solving the linear system, as investigated by Thormann et. al.[27]

Nevertheless, the amount of GMRES-restart vectors used to drive the LFD simulations in fig. 3 are found

Table 2. Varying computation parameters for the Krylov-GMRES method over reduced frequency with constant weighting factor $\xi = 0.5$ between first and second order flux Jacobian for the LFD.

Case	# restart vectors	# ILU steps	k [-]
derivative, lower k	60	3	0.1
baseline	60	3	0.2
derivative, intermediate k	170	3	0.4
derivative, intermediate k	185	5	0.6
derivative, intermediate k	210	5	0.8
derivative, highest k	210	5	1.0

in table 2 which steeply rise for reduced frequencies at 0.4 and higher. Thus, related to LFD simulations with detached flow conditions, memory issues play a major role for successfully applying the LFD method. Throughout the LFD simulations for transonic and separated flows, preconditioning steps has been altered from 3 to a maximum of 5 steps. More than 5 preconditioning steps slows down the simulation considerably and in most of the cases a more robust convergence could not be achieved.

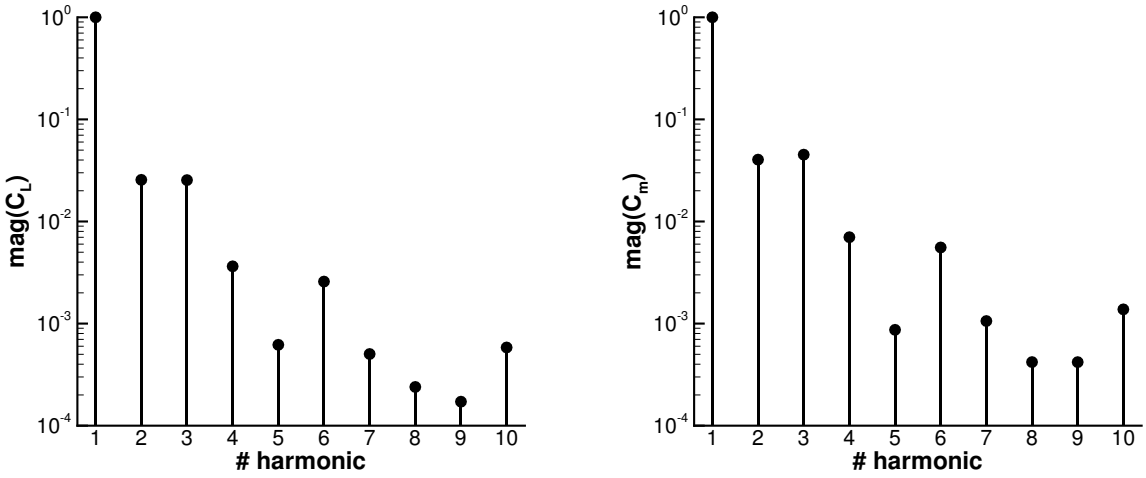

(a) $|\widehat{C}_L|$ (b) $|\widehat{C}_m|$

Figure 4. Extraction of the first ten harmonics of the magnitude of C_L (a) and C_m (b) of the URANS simulation for the Lann CT9 baseline configuration. C_L and C_m are normalized with the magnitude of the first harmonic.

The LFD is dependent on the assumption that only the first harmonic is from importance. One way to meet this condition, is to chose the input amplitude of the forced motion very small but it does not guarantee its general applicability. To give an idea about higher harmonics, fig. 4 presents the extraction of higher harmonics of the time signal for the magnitude of $|\widehat{C}_l|$ (a) and $|\widehat{C}_m|$ (b) of the URANS simulation for the baseline case. Overall, the magnitudes decrease steadily with higher harmonics. Both coefficients nearly reveal the same decay characteristics. An exponential decay of higher harmonics is not guaranteed which is an assumption for applying the small disturbance approach. The difference between the first and second harmonic is in both figures about 1.5 orders of magnitude which supports the presumption of considering only the first harmonic for that specific case. Higher harmonics would gain non-negligible influence on the time signal if they are within the same order as the first harmonic.

III.A. Verification of linearized right-hand side vector

Figure 5 displays the absolute error in the cut plane at $y/s = 0.65$ and on the surface of the wing between central finite difference (FD), with an applied step size of $\epsilon = 1 \times 10^{-5}$, and linearized right-hand side vector defined in Eq. (4). The discrete field resolution achieves a second order accuracy. Figures 5(a) and 5(c) show

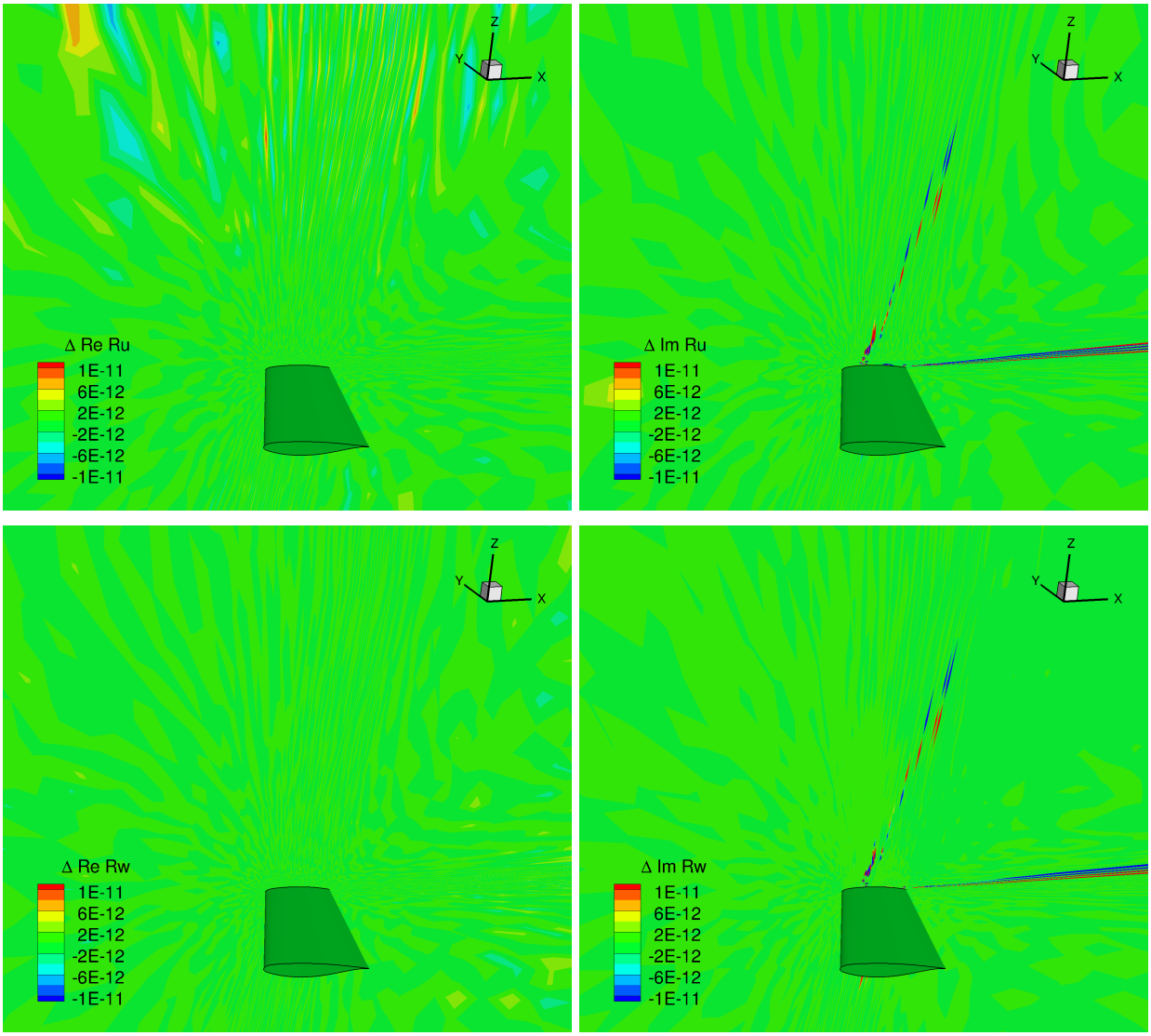

Figure 5. Absolute difference between central finite differencing (FD, $\epsilon = 1 \times 10^{-5}$) and analytic linearization of right-hand side variables for the equivalent velocity residuals, column-wise Re Ru, Re Rw and Im Ru, Im Rw, at span station $y/s = 0.65$ and on the surface of the wing.

a rising error from the airfoil outward. With one finite difference epsilon used for the pitch motion where the bearing is chosen to be near the midspan of the wing, the FD-step size epsilon is equivalent to an angle which increases naturally from the wing outwards. Only the imaginary part in figs. 5(b) and 5(d) visualizes negligible local absolute errors ($\approx 5 \times 10^{-10}$) near the wing between both methods, overlying with the shock location and the wake of the wing. Not only the complexity of the flow introduces these errors, instead the clustering and skewed structured grid in that regions is jointly responsible for the differences.

Table 3. Comparison of C_L and C_m derivatives obtained from the right-hand side with analytic differentiation and central finite differencing (FD) for a pitch motion, FD-step size $\epsilon = 1 \times 10^{-5}$.

	Real	Imag
Coefficient	C_L	
FD	-0.03346259767452	0.11593903371636
Analytic	-0.03346254574405	0.11566451532539
Diff.	-0.00000005193047	0.00027451839097
Coefficient	C_m	
FD	-0.00177636773872	-0.09770097632011
Analytic	-0.00177638959493	-0.09746784772746
Diff.	0.00000002185621	-0.00023312859265

Table 3 compares C_L and C_m in absolute errors between central finite difference (FD) and linearized right-hand side vector. The linearized real part of the coefficients achieve more than first order accuracy, under the premise of testing a three-dimensional case. The accuracy gain of the linearized right-hand side appraoch is clearly visible for the corresponding imaginary part of the coeffcients.

III.B. Surface pressure and skin friction distribution

To verify the prediction quality of the LFD method for separated flows, the obtained first harmonic pressure ($\hat{c}_p$) and skin friction ($\hat{c}_f$) coefficients are compared to those of the URANS at two distinct span locations.

Figure 6 upper row shows the time-invariant mean pressure coefficient for both span locations at $y/s = 0.2$ and $y/s = 0.65$. At $y/s = 0.2$, fig. 6 (a), the $\bar{c}_p$ on the suction side differ widely between the experiments and the URANS data. The shock strength and location is not well resolved which opens a fruitful discussion for the turbulence model in use. The steady-state c_p and c_f and the URANS mean $\bar{c}_p$ and $\bar{c}_f$ match exactly in fig. 6 (a) and (c). However, deviations in the shock location can be observed when comparing the steady-state and mean surface pressure for the baseline excitation ($\hat{\alpha} = 0.25\,\mathrm{deg}$). For c_p as well as c_f, the shock is smoothed indicating a strong motion and nonlinearities. When using a smaller excitation amplitude, the steady-state and mean of c_p and c_f is resolved equally good. Only slight deviations can be seen for $\bar{c}_p$ at $y/s = 0.65$, fig. 6 (b), between experiment and the URANS simulation for the baseline configuration. The same behavior, a more flattened shock is detected for the skin friction in fig. 6 (d) at the shock position for the baseline excitation. The strong shock induced separation appears at the outer part of the wing from $x/c \approx 0.4$ downstream to the trailing edge, fig. 6 (d), indicated with $\bar{c}_f < 0$.

The prediction quality of the dynamic response data for pressure and viscous forces can be predetermined by the comparison of the complex-valued $\hat{c}_p$ and $\hat{c}_f$ between the LFD and URANS method. Figure 7 presents the real and imaginary part of $\hat{c}_p$ at the span location $y/s = 0.2$, upper row, and $y/s = 0.65$ lower row. Regarding the shock strength at $y/s = 0.65$ in figs. 7(c) and 7(d), the prediction of $\mathrm{Re}(\hat{c}_p)$ and $\mathrm{Im}(\hat{c}_p)$ between experiment and URANS is opposite but the streamwise alignment is in good agreement. The important comparison is between the LFD and URANS simulations for the lower excitation amplitude of $\hat{\alpha} = 0.01\,\mathrm{deg}$. Both $\mathrm{Re}(\hat{c}_p)$ and $\mathrm{Im}(\hat{c}_p)$ at $y/s = 0.2$ and $y/s = 0.65$ agree excelently in figs. 7(a) to 7(d). Although, the URANS results for the baseline and lower excitation at the outer wing section, figs. 7(c) and 7(d), differ in the shock region, the integrated loads are not affected significantly, since the enclosed area under the bell-shaped graph of the shock region is approximately equivalent for both URANS solutions. Therefore, the shock impulse is preserved as found by Lindquist and Giles.[29]

A similar description applies for the real and imaginary part of the surface skin friction coefficient in all four figs. 8(a) to 8(d). There are no experimental data available and thus, only numerical results can be

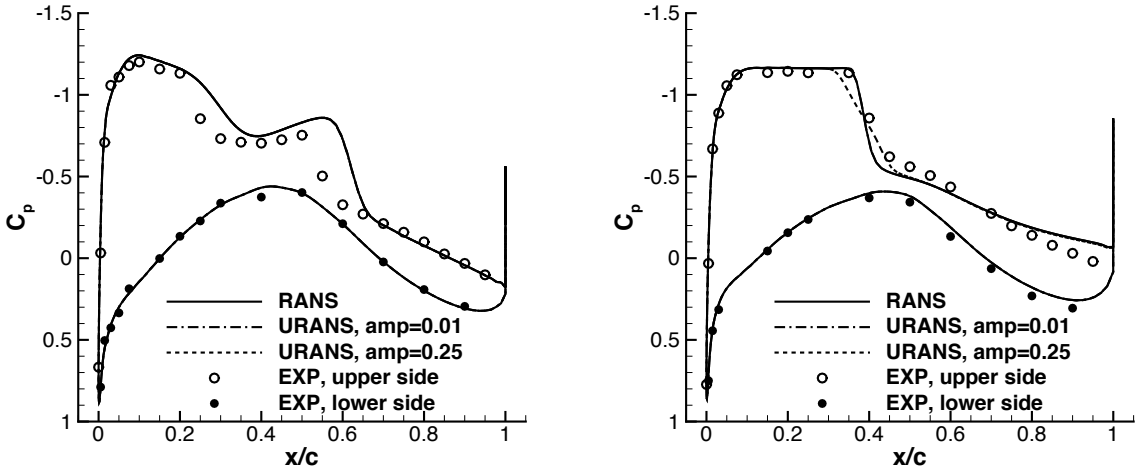

(a) $c_p, \bar{c}_p,\ y/s = 0.2$

(b) $c_p, \bar{c}_p,\ y/s = 0.65$

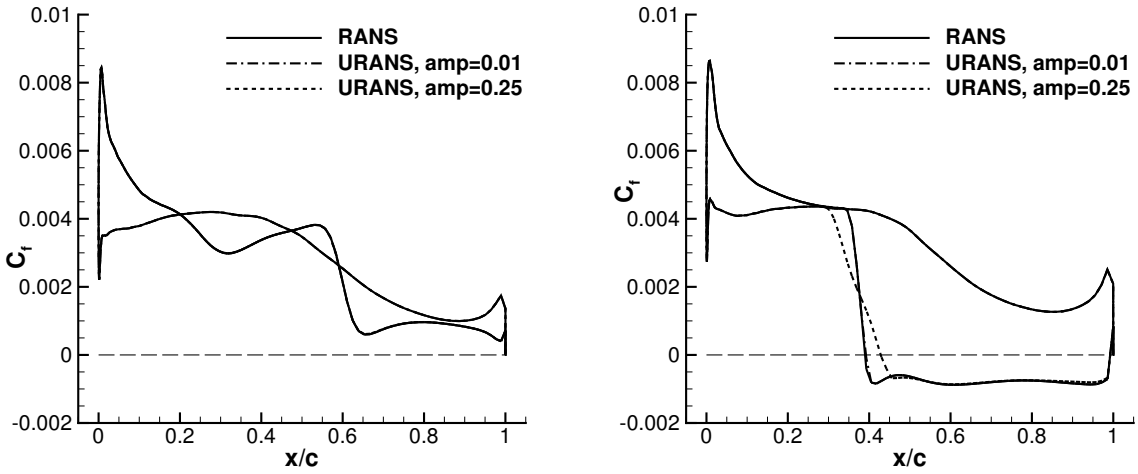

(c) $c_f, \bar{c}_f,\ y/s = 0.2$

(d) $c_f, \bar{c}_f,\ y/s = 0.65$

Figure 6. Comparison between the RANS obtained steady pressure coefficient distribution (c_p, the LFD time-invariant mean) for the LANN CT9 wing at $\mathrm{M}_\infty = 0.82, \mathrm{Re}_\infty = 7.3 \times 10^6, \bar{\alpha} = 2.6\,\mathrm{deg}$ and the URANS obtained mean $\bar{c}_p$ as well as with experimental data[24] (upper row) at two span stations $y/s \in 0.2, 0.65$, comparison of the RANS obtained steady skin friction coefficient distribution c_f for the precedingly given steady cases (lower row).

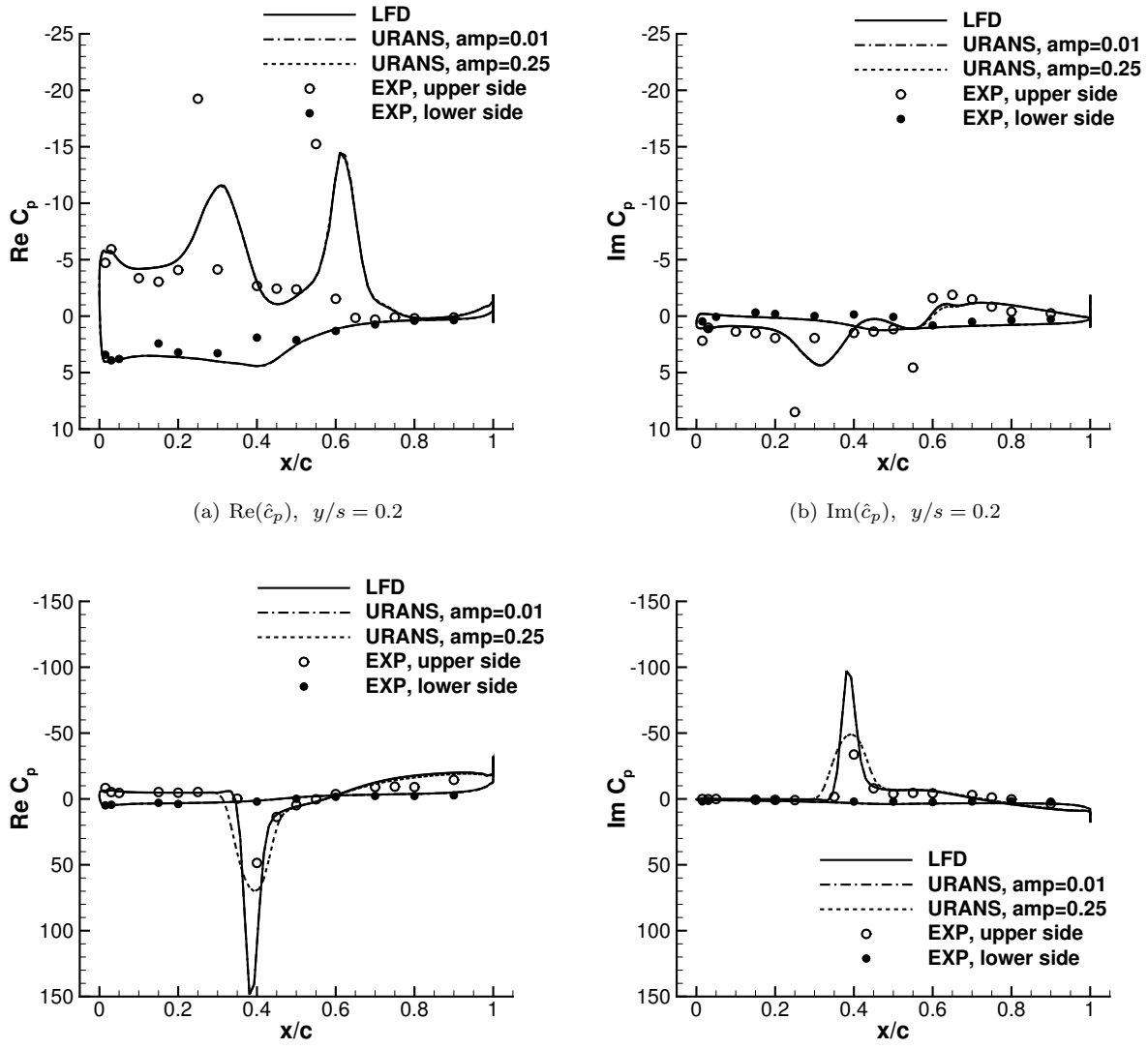

(a) $\mathrm{Re}(\hat{c}_p)$, $y/s = 0.2$

(b) $\mathrm{Im}(\hat{c}_p)$, $y/s = 0.2$

(c) $\mathrm{Re}(\hat{c}_p)$, $y/s = 0.65$

(d) $\mathrm{Im}(\hat{c}_p)$, $y/s = 0.65$

Figure 7. Comparison of the LFD, URANS and experimentally obtained real and imaginary part of the first harmonic pressure coefficient distribution ($\mathrm{Re}(\hat{c}_p)$ and $\mathrm{Im}(\hat{c}_p)$) for the LANN wing CT9 baseline at two span stations: $y/s \in 0.2, 0.65$. The derivative case $\hat{\alpha} = 0.01\,\mathrm{deg}$, is also included.

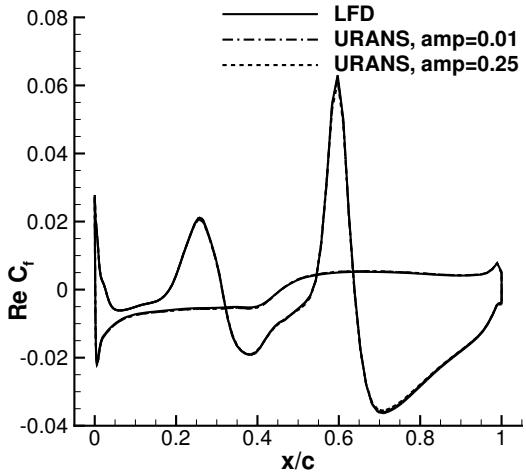

(a) $\mathrm{Re}(\hat{c}_f)$, $y/s = 0.2$

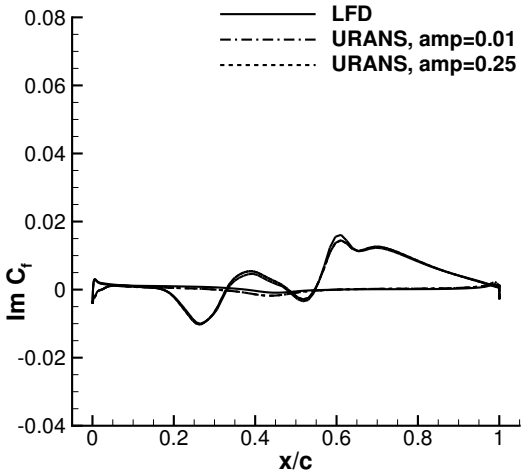

(b) $\mathrm{Im}(\hat{c}_f)$, $y/s = 0.2$

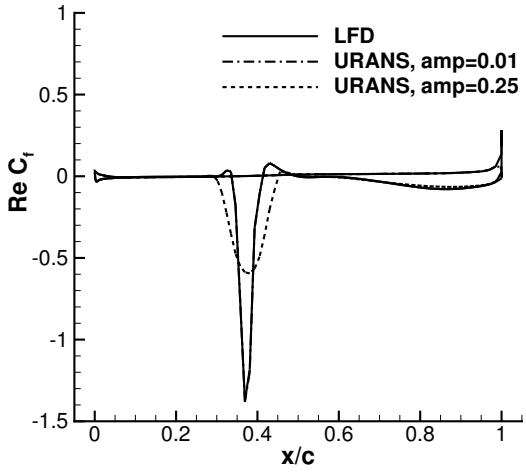

(c) $\mathrm{Re}(\hat{c}_f)$, $y/s = 0.65$

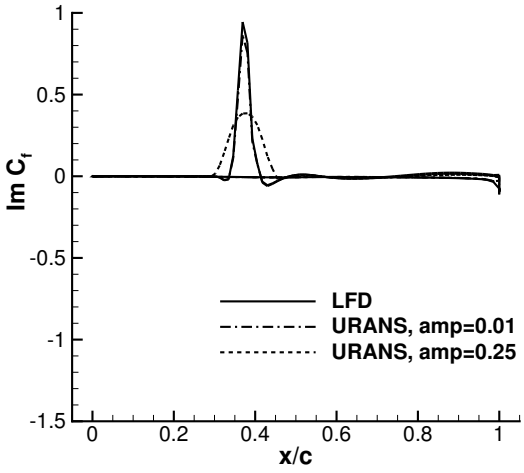

(d) $\mathrm{Im}(\hat{c}_f)$, $y/s = 0.65$

Figure 8. Comparison of the LFD and URANS obtained real and imaginary part of the first harmonic skin friction coefficient distribution ($\mathrm{Re}(\hat{c}_f)$ and $\mathrm{Im}(\hat{c}_f)$) for the LANN wing CT9 derivative case ($\hat{\alpha} = 0.01\,\mathrm{deg}$) at two span stations: $y/s \in 0.2, 0.65$.

compared. The computed $\hat{c}_f$ is approximately two orders of magnitude smaller than $\hat{c}_p$, which is caused by the high Reynolds number. Hence, the influence of viscous forces is considered to be negligible. The real part of c_f (Re($\hat{c}_f$), y/s=0.2) on the upper side in fig. 8(a) has a similar characteristic to its pressure counterpart in fig. 7(a) regarding strength of peaks. However, the Re($\hat{c}_f$) peaks are relocated further downstream than $\hat{c}_p$. A similar behavior appears for both upper and lower side of the wing between Im($\hat{c}_f$), fig. 8(b), and Im($\hat{c}_p$), fig. 7(b). At $y/s = 0.65$ an almost identical behavior occurs between both complex-valued forces (figs. 7(c) and 7(d),figs. 8(c) and 8(d)), with a coincide location of the peaks. Viscous forces are predicted good, since a good agreement is obtained between the LFD and URANS results for the lower excitation amplitude.

III.C. Frequency Response Function

Magnitude and phase of the dynamic response data are compared between LFD and URANS. The frequency dependency for both cases are investigated for oscillation in pitch and plunge.

Table 4. Computation parameters for the LANN wing CT9 baseline and the considered derivative cases.

Case	$\hat{\alpha}/\hat{h}$ [deg/-]	k [-]
baseline	0.25	0.2
derivative, pitch, FRF	0.01	0.001-1.0[a]
derivative, pitch/plunge, ARF	0.001-1.0[b]	0.2
derivative, plunge, FRF	0.001	0.001-1.0[a]

[a] incremental, 10 instances together

[b] incremental, 5 instances together

Table 4 lists the performed test cases. Amplitude repsponse function (ARF) and frequency response function (FRF) cases spanning three order of magnitude in in excitation amplitude and k, respectively, for both methods for magnitude and phase of C_L and C_m. Next to the LANN CT9 baseline case, three derivative cases at lower $\hat{\alpha}$, yet of equal or higher k, are simulated as well.

The influence of the excitation amplitude, fig. 9, has been analyzed for the reduced frequency $k = 0.2$ for a motion in pitch and plunge. Displayed are magnitudes and phase shifts of the first harmonic of the lift and moment coefficient versus a log-scaled excitation amplitude (ARF). The LFD method does not incorporate an excitation amplitude and is therefore independent of $\hat{\alpha}$. The obtained values are scaled with the excitation amplitude to be comparable with the URANS results. Units of the excitation amplitude are in degrees for $\hat{\alpha}$ for motion in pitch, and grid units are used for plunge. Thus, the maximum excitation for the ARF range is one degree for pitch, and becomes one grid unit equivalent to about 1.6 times the wings reference length for plunging. All ARFs obtained with the URANS method for $\widehat{C}_L$ and $\phi_{\widehat{C}_L}$, figs. 9(a) and 9(c), as well as $\widehat{C}_m$ and $\phi_{\widehat{C}_m}$, figs. 9(b) and 9(d), are invariant until $\hat{\alpha} <= 0.1$, which verifies the dynamically linear behavior over the perturbation amplitude. URANS obtained ARFs for the magnitude and phase lag in fig. 9, exhibits a deviation from being dynamical linear to dynamically nonlinear above $\hat{\alpha} > 0.1$, except for the phase of both coefficients for the plunge motion. That ascertains the chosen URANS amplitude of $\hat{\alpha} = 0.01$ deg for the pitch motion. An appropriate excitation amplitude for the plunging motion has been chosen in accordance with the pitching amplitude. Thus, a similar maximum deflection for plunge results in an excitation of about one order less then $\hat{\alpha} = 0.01$ deg and thus is $\hat{h} = 0.001$.

FRF plots are shown in fig. 10 for an harmonic pitch and plunge motion. The comparison between LFD and URANS simulations agree well in all four figures. A general view of the four figures, fig. 10, does show neither any severe outlier nor any qualitative different shape of the plots. For the rotational (pitch) motion and for infinitesimal frequencies ($f \to 0$), the magnitude of both coefficients approach the low frequency asymtote, referred as the steady-state static derivative. It reaches approximately 2 for the magnitude of C_L, and for C_m about 0.6. Steady-state static derivatives for translational (plunge) motions are zero, figs. 10(c) and 10(d). The phase for C_L for pitch and plunge are in a narrow band in figs. 10(a) and 10(c). The $\phi_{\widehat{C}_L}$ is between 0 deg to 40 deg for pitch, and the $\phi_{\widehat{C}_L}$ for plunge is between 60 deg and 130 deg. However, the range for $\phi_{\widehat{C}_m}$ is enormous for both motions, including a zero crossing of the phase for plunging. For pitch, the range of $\phi_{\widehat{C}_m}$ is between ≈ 45 deg and -180 deg, and for plunge it is between 90 deg to ≈ -120 deg.

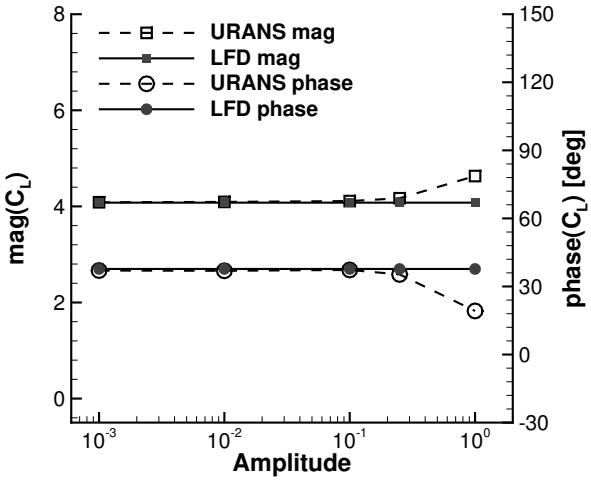

(a) ARF, $\bar{\alpha} = 2.6$ deg, $k = 0.2$, pitch

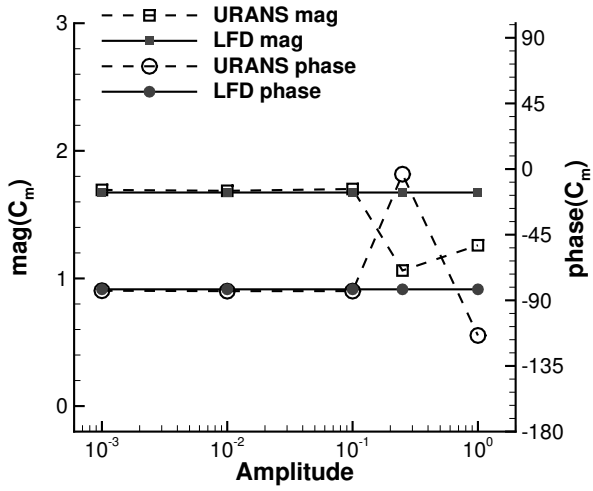

(b) ARF, $\bar{\alpha} = 2.6$ deg, $k = 0.2$, pitch

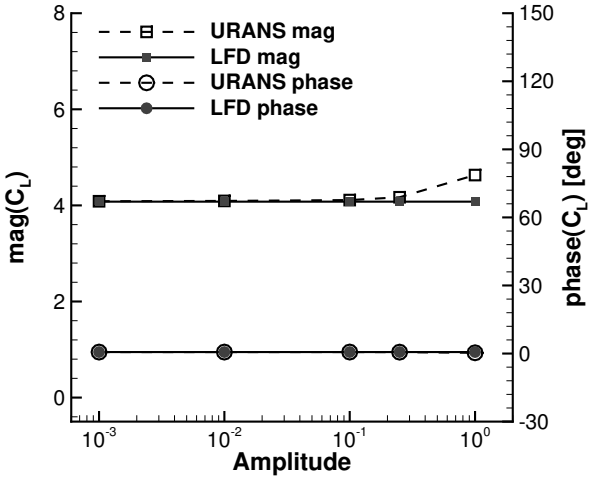

(c) ARF, $\bar{\alpha} = 2.6$ deg, $k = 0.2$, plunge

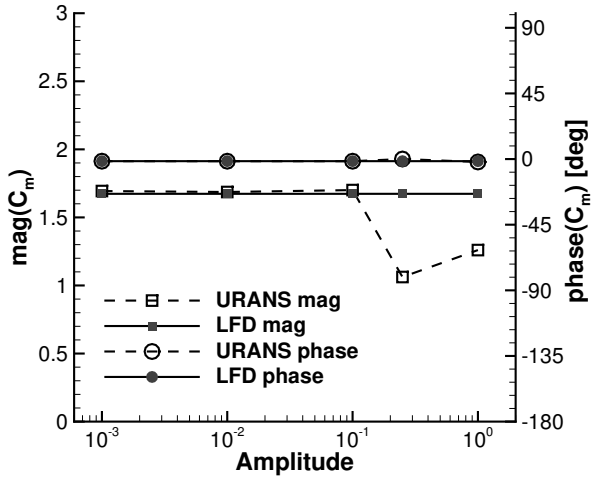

(d) ARF, $\bar{\alpha} = 2.6$ deg, $k = 0.2$, plunge

Figure 9. Comparison of the LFD and URANS obtained amplitude lift and pitching moment coefficient's magnitude and phase for the LANN CT9 baseline case undergoing a pitch motion ((a) and (b)) and plunge motion ((c) and (d)), ARF cases.

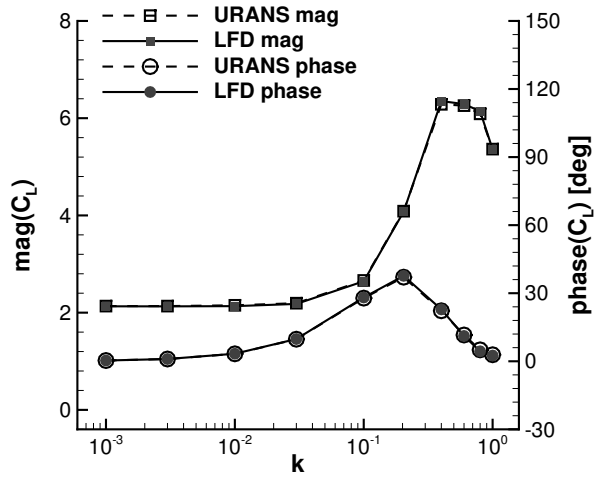

(a) FRF for C_L, $\hat{\alpha} = 0.01\,\text{deg}$, pitch

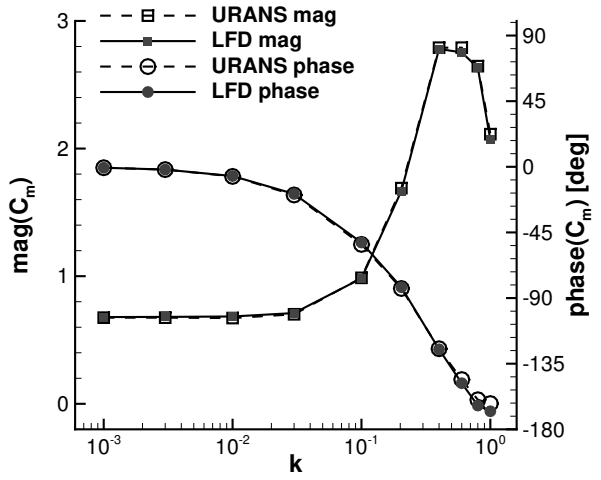

(b) FRF for C_m, $\hat{\alpha} = 0.01\,\text{deg}$, pitch

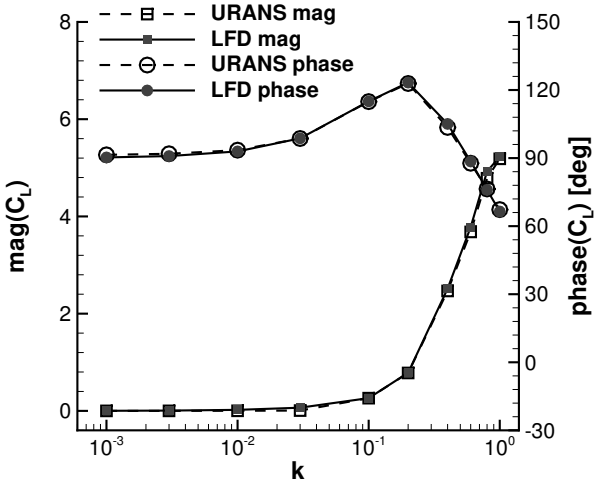

(c) FRF for C_L, $\hat{h} = 0.001$, plunge

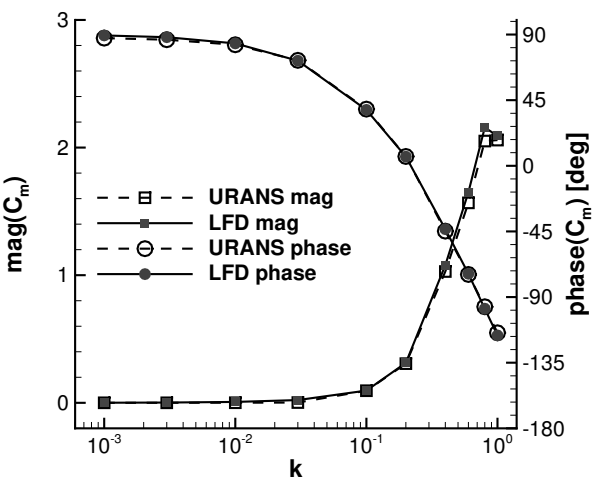

(d) FRF for C_m, $\hat{h} = 0.001$, plunge

Figure 10. Comparison of the LFD and URANS obtained lift and pitching moment (C_L and C_m) coefficient's magnitude and phase for the LANN CT9 case undergoing a pitch (a),(b) and plunge (c),(d) motion, lower $\hat{\alpha} = 0.01\,\text{deg}$ as well as $\hat{h} = 0.001$, FRF cases.

The same trend of the phase for C_L for pitch and plunge is noticeable in figs. 10(a) and 10(c), as well as for C_m (figs. 10(b) and 10(d)). The phase lead of $\phi_{\widehat{C}_L}$ and $\phi_{\widehat{C}_m}$ increases continuously until reaching the maximum at $k = 0.2$. $\phi_{\widehat{C}_L}$ then drops almost to zero, and $\phi_{\widehat{C}_m}$ decreases to a minimum of about 70 deg, which is below its low frequency asymtote of 90 deg. A similar characteristic is observed for the magnitudes of C_L and C_m, figs. 10(a) and 10(b), for the motion in pitch, and for C_L and C_m in figs. 10(c) and 10(d) for plunging. Furthermore, after a steep rise of the magnitudes of C_L and C_m for pitch, it reaches a maximum between $k = 0.4$ to $k = 0.6$, followed by a steep drop. Certain disagreement appears for the magnitude of C_m for pitch and plunge, as evident in figs. 10(b) and 10(d), for higher k values and for the phase of C_m, fig. 10(b), for the pitch motion only.

Table 5. Relative and absolute errors for FRFs over all k instances of magnitude and phase for C_L and C_m for both pitching and plunging LANN CT9. AbsError = $\hat{C}_{URANS} - \hat{C}_{LFD}$, RelError = $(1 - \hat{C}_{LFD}/\hat{C}_{URANS}) \times 100$.

	pitch, $\hat{\alpha} = 0.01$ deg		plunge, $\hat{h} = 0.001$	
	AbsError min/max	RelError, % min/max	AbsError min/max	RelError, % min/max
$\lvert\widehat{C}_L\rvert$	-0.017/0.067	-0.8/1.1	< 0.001/0.140	0.4/2.9
$\phi_{\widehat{C}_L}$	-0.63/0.61	-12.5/2.8	-1.1/1.5	-1.2/1.5
$\lvert\widehat{C}_m\rvert$	-0.045/0.0125	-2.1/1.9	< 0.001/0.106	1.0/5.3
$\phi_{\widehat{C}_m}$	-5.27/1.28	-4.0/3.2	1.8/1.9	-3.0/2.1

Table 5 quantifies relative and absolute errors over the investigated k range for pitch and plunge motion. Magnitudes for both coefficients are predicted within an acceptable accuracy. The minimum and maximum $\phi_{\widehat{C}_L}$ may seem to be far off since relative errors of -12.5% occur at $k = 0.8$ and 2.8% at $k = 0.6$, respectively, but their difference in absolute errors are insignificant because $\phi_{\widehat{C}_L}$ approaches zero for the highest k values. Below $k = 0.6$, $\phi_{\widehat{C}_L}$ is predicted with less than 1.6 %, and the difference decreases further with decreasing k. This is similar for the phase of C_m, which is less than one percent below $k = 0.6$. The prediction quality is more accurate over a larger range for the phase for plunging between both methods. It is well below one percent for the $\phi_{\widehat{C}_L}$ for $k < 0.8$. The minimum difference occurs at $k = 0.6$ and the maximum at the smallest k of 0.001, again while appraoching the low frequency asymtote of zero. The prediction of $\phi_{\widehat{C}_m}$ is below 1.5 percent overall except for the minimum at $k = 1$ and the maximum appears at $k = 0.4$. Most outliers occur at higher k values, although it is more error prone to provide reliable data for these k values with URANS for the detached flow of case CT9.

III.D. Computational Efficiency

The key-benefit of a LFD solver is the commonly established efficiency gain in comparison to non-linear URANS simulations. During the validation process required CPU-time was assessed to substantiate the realizable CPU-time reduction of LFD-TAU and its URANS counterpart.

Table 6. Quantitative comparison on the computational effort involved with the URANS and LFD (ILU, GMRES, sg) simulation for the LANN wing case CT9, as well as the derived CPU-time reduction factor ($\zeta_{CPU} := CPU\text{-}time\ URANS/CPU\text{-}time\ LFD$).

	simulation CPU-time (h)			
Case	URANS	LFD	CPU's	ζ_{CPU}
LANN Wing CT5[20]				
baseline, 3 periods, LU-SGS, 3V-mg, GMRES	389	62.6	8/16	6.2
baseline, 3 periods, ILU, GMRES, sg	389	4.4	8/24	88
LANN Wing CT9				
baseline, 4 periods, ILU, GMRES, sg	5512	32	24/24	174

Table 6 lists the CPU-times for selected URANS and LFD simulations as well as the derived CPU-time reduction factor. In addition, the number of computed periods in the URANS simulation as well as the

number of utilized processors are given. The CPU times of the LFD and URANS simulations are scaled with the number of processors, assuming linear speed-up of parallelization. Since only one solver method has been used for the CT9, the data is compared to previous CPU time investigations for the case CT5 with attached flow.[20] The residual abort criterion was set to 10^{-5} for all LFD simulations.

The CPU time reduction factors for the LANN CT5 and CT9 baseline simulations improve considerably by using advanced preconditioning methods. Employing the ILU as a preconditioner for the Krylov-GMRES solver yields a CPU time reduction factor 88 as opposed to 6.2 for the common LU-SGS, 3V-mg solver. A time reduction factor of 174 is achieved for the case CT9. Considering the memory requirement for the CT9 baseline case with 60 GMRES restart vectors, a multiple of approx. 15 was necessary in comparison to the RANS method (approx. 1.7 GB), and reached approx. 20 with 210 GMRES restart vectors.

The number of computed periods and the termination criterion employed in the dual time stepping scheme of the URANS simulations have a significant influence on the CPU time reduction factor. Typically, CPU-time reduction factors of more than an order of magnitude can be achieved with a LU-SGS and a Krylov-GMRES solver. Two orders of magnitude can be obtained using an ILU preconditioning with the latter solver.

IV. Conclusions

This paper presents a robust and accurate linearized method based on RANS equations for predicting unsteady air loads for the challenging transonic flow conditions at the edge of the flight envelope. The chosen test cases provide shock-induced separation and shock flow conditions for which the LFD method predicts dynamic air loads comparably well to its counterpart URANS. It is a robust and mature method for complex applications by using a mixed first and second order flux Jacobian ILU pre-conditioning technique for the GMRES approach but can drive the memory requirements beyond limits under certain situations. Favorable time saving factors of up to two order of magnitude for separated transonic flow conditions compared to nonlinear time-accurate simulations introduces the LFD method as an efficient alternative for harmonic oscillations with small excitation amplitudes.

Another substantial part for the LFD method is the consistent linearization of the complete Navier-Stokes equations including the turbulent transport equation for the Spalart-Allmaras working variable. A gained experience with those test cases has shown that slight inconsistencies in the linearization, i.e. simplifications in the flux evaluation routines, can prevent convergence of the LFD method or residual stalling after a few orders of magnitude. The combination of consistent linearizations of the flow solvers flux routines and the use of the mixed 1^{st} and 2^{nd} order ILU-preconditioner enables the general use of the LFD method for a wide range of applications. The preconditioner has the most influence on a robust method for solving the linear system of equations. The main trade-off appears for the LFD in correlation with high memory consumption and many core architectures, since memory requirements for the proposed ILU-preconditioning and the storage of the flux Jacobian for solving the linear system is an order of magnitude higher than the comparable nonlinear flow solver. Another issue for a successful application of the LFD is a well converged flow simulation. The derivation of the equation for the LFD inherently sets the flow residual to zero. In practice this condition is often not fulfilled. It has been demonstrated for attached cases, for example the LANN CT5, that this condition can be handled more loose. In the present case, LANN CT9, no results were obtained with the LFD whenever the flow residual convergence did not reach at least ten orders of magnitude. The drawback for evaluating the right-hand side vector with central finite differences has been resolved by linearization of the grid-node coordinate and grid-node velocity dependent discrete residual and dual grid metric. Efficiency is secondary if applied for a frequency band for one motion, because the right-hand side needs to be evaluated only once, but the accuracy gain is the main reason.

Further improvement in robustness can be expected by using the viable GMRES-method with its continuous enhancements such as recycling[30] or pipelining extensions. Paralellisation of the preconditioner is another major performance issue but is encountered as a challenging task because improper implementation can generate a bottleneck in communication. The basic equation for rigid body motion can also be replaced by a general grid deformation and its consecutive linearization, which become necessary for elastically deformed bodies.

Appendix

Change of state vector

The primitive flow state vector is defined as

$$\begin{aligned}\mathbf{W}_p &:= [\rho, u, v, w, p, \check{\nu}]^T, \\ p &= (\gamma-1)(\rho E - \frac{1}{2\rho}\left\|\rho\mathbf{U}\right\|^2), \\ \rho E &= \frac{p}{\gamma-1} + \frac{1}{2\rho}\left\|\rho\mathbf{U}\right\|^2, \quad \frac{1}{2\rho}\left\|\rho\mathbf{U}\right\|^2 = \frac{1}{2\rho}\left((\rho u)^2 + (\rho v)^2 + (\rho w)^2\right).\end{aligned} \tag{17}$$

and the conservative flow state vector is $\mathbf{W}$. The derivative of primitive flow variables with respect to conservative flow variables is

$$\frac{\partial \mathbf{W}_p}{\partial \mathbf{W}} = \begin{bmatrix} 1 & 0 & 0 & 0 & 0 & 0 \\ -\frac{u}{\rho} & \frac{1}{\rho} & 0 & 0 & 0 & 0 \\ -\frac{v}{\rho} & 0 & \frac{1}{\rho} & 0 & 0 & 0 \\ -\frac{w}{\rho} & 0 & 0 & \frac{1}{\rho} & 0 & 0 \\ \phi & -(\gamma-1)u & -(\gamma-1)v & -(\gamma-1)w & \gamma-1 & 0 \\ -\frac{\check{\nu}}{\rho} & 0 & 0 & 0 & 0 & \frac{1}{\rho} \end{bmatrix}, \tag{18}$$

with $\phi = (\gamma-1)(u^2+v^2+w^2)$.

Linearization of the skin friction coefficient

For obtaining $\hat{c}_f$, Eq. (14) and Eq. (13), on a viscous wall, differentiation with the chain rule results in

$$\begin{aligned}\hat{c}_f = \frac{\partial c_f}{\partial \alpha} &= \begin{bmatrix} \mathrm{Re}\, c_f \\ \mathrm{Im}\, c_f \end{bmatrix} = \\ &= \frac{2}{\rho_\infty U_\infty^2}\left(\frac{\partial \mathrm{sgn}(u_{n_p})}{\partial \alpha}\mu_{\text{eff}}\left\|\nabla\times\mathbf{U}\right\| + \right. \\ &\quad \left. + \mathrm{sgn}(u_{n_p})\frac{\partial \mu_{\text{eff}}}{\partial \alpha}\left\|\nabla\times\mathbf{U}\right\| + \mathrm{sgn}(u_{n_p})\mu_{\text{eff}}\frac{\partial\left\|\nabla\times\mathbf{U}\right\|}{\partial\alpha}\right).\end{aligned} \tag{19}$$

The first derivative with $\mathrm{sign}(u_{n_p})$ is constant, thus it equals zero, and the derivative simplifies to

$$\hat{c}_f = \mathrm{sgn}(u_{n_p})\frac{2}{\rho_\infty U_\infty^2}\left(\frac{\partial \mu_{\text{eff}}}{\partial\alpha}\left\|\nabla\times\mathbf{U}\right\| + \mu_{\text{eff}}\frac{\partial\left\|\nabla\times\mathbf{U}\right\|}{\partial\alpha}\right). \tag{20}$$

Differentiating the effective viscosity introduces the laminar and turbulent eddy viscosity based on Spalart-Allmaras turbulence transport-equation.[25] Linearization of effective viscosity yields

$$\begin{aligned}&\mu_{\text{eff}} := \mu_l + \mu_t, \quad \mu_{\text{eff}}(t,\mathbf{x}) := \bar{\mu}_{\text{eff}}(\bar{\mathbf{x}}) + \tilde{\mu}_{\text{eff}}(t,\mathbf{x}), \\ \text{S-A}: \quad &\mu_t := \mu_t(\rho\check{\nu}), \quad \mu_t|_b \equiv 0, \quad \left.\frac{\partial \mu_t}{\partial \mathbf{W}}\right|_{b,\overline{\mathbf{W}}} \equiv 0\,. \\ n_h = 1: \quad &\tilde{\mu}_{\text{eff}} = \hat{\mu}_{\text{eff}}e^{i\omega t} = \left.\frac{\partial \mu_{\text{eff}}}{\partial \mathbf{W}}\right|_{\overline{\mathbf{W}}}\widehat{\mathbf{W}}e^{i\omega t} = \left(\left.\frac{\partial \mu_l}{\partial T}\right|_{\bar{T}}\hat{T} + \left.\frac{\partial \mu_t}{\partial \mathbf{W}}\right|_{\overline{\mathbf{W}}}\widehat{\mathbf{W}}\right)e^{i\omega t}.\end{aligned} \tag{21}$$

where μ_l and $\partial\mu_l/\partial T$ is described as

$$\mu_l := \mu_l(T), \quad \mu_l = \mu_{l,\infty}T^{\frac{3}{2}}\left[\frac{1+S}{T+S}\right], \tag{22}$$

$$\frac{\partial \mu_l}{\partial \mathbf{W}_p} \equiv \frac{\partial \mu_l}{\partial T} = \mu_{l,\infty}T^{\frac{3}{2}}\left(\frac{1+S}{T+S}\right)\left[\frac{1}{T+S}\left(\frac{3(T+S)}{2T} - 1\right)\right], \tag{23}$$

and $\mu_{l,\infty}$ is the freestream molecular viscosity. In principle, differentiation with the chain rule to obtain $\hat{\mu}$ reads like

$$\hat{\mu} = \frac{\partial \mu}{\partial \alpha} = \frac{\partial \mu}{\partial \mathbf{W}_p} \frac{\partial \mathbf{W}_p}{\partial \mathbf{W}} \frac{\partial \mathbf{W}}{\partial \alpha}, \quad \frac{\partial \mathbf{W}}{\partial \alpha} \equiv \widehat{\mathbf{W}}. \tag{24}$$

Since the skin friction coefficient uses the magnitude of the vorticity, $\omega = \nabla \times \mathbf{U}$, its linearization is derived as

$$\begin{aligned} \omega &= \bar{\omega} + \tilde{\omega}, \quad \tilde{\omega} = \left.\frac{\partial \omega}{\partial \mathbf{U}}\right|_{\bar{\mathbf{U}}} \widetilde{\mathbf{U}}, \\ \widehat{\|\omega\|} &= \frac{\partial \|\omega\|}{\partial \alpha} = \frac{\partial \|\omega\|}{\partial \mathbf{W}_p} \frac{\partial \mathbf{W}_p}{\partial \mathbf{W}} \frac{\partial \mathbf{W}}{\partial \alpha}, \quad \frac{\partial \|\omega\|}{\partial w_k} = \frac{\partial \|\omega\|}{\partial \omega} \frac{\partial \omega}{\partial \nabla \mathbf{U}} \frac{\partial \nabla \mathbf{U}}{\partial \mathbf{U}}. \end{aligned} \tag{25}$$

References

[1]Bryan, G. H., *Stability in Aviation*, MacMillan and Co., Limited, London, 1911.

[2]Etkin, B. and Reid, L. D., *Dynamics of Flight*, J. Wiley & Sons, Inc, 3rd ed., 1996.

[3]Valensi, J., "A review of the techniques of measuring oscillatory aerodynamic forces and moments on models oscillating in wind tunnels in use on the continent," General Assembly AG 15/P6, AGARD 4, 1955.

[4]Schmidt, E., "Über die Messung instationärer flugmechanischer Derivativa im Windkanal," Tech. Rep. 0271, DFL-Bericht, Braunschweig, Germany, 1964.

[5]Hübner, A. R., Bergmann, A., and Löser, T., "Experimental and numerical investigations of unsteady pressure distributions and aerodynamic forces on moving transport aircraft configurations." AIAA-2009-0091, Orlando, Florida, June 2009.

[6]Newsom, J. R. and Pototzky, A. S., "Analysis and Flight Data for a Drone Aircraft with Active Flutter Suppression," *Journal of Aircraft*, Vol. 19, No. 11, 1981, pp. 1012–1018. doi: 10.2514/3.44805.

[7]Brendes, G. and Voß, R., "Transonic flutter calculations for a low wing transport aircraft using the Transonic Doublet Lattice Method," *10th International Forum for Aeroelasticity and Structural Dynamics*, IFASD Paper 2001-, Madrid, Spain, June 2001, LIDO-Berichtsjahr 2001,.

[8]Clark, W. S. and Hall, K. C., "A Time-Linearized Analysis of Stall Flutter," *Journal of Turbomachinery*, Vol. 122, No. 3, 2000, pp. 467–476. doi: 10.1115/1.1303073.

[9]McMullen, M., Jameson, A., and Alonso, J. J., "Demonstration of Nonlinear Frequency Domain Methods," *AIAA Journal*, Vol. 44, No. 7, July 2006, pp. 1428–1435. doi: 10.2514/1.15127.

[10]Limache, A. C. and Cliff, E. M., "Aerodynamic Sensitivity Theory for Rotary Stability Derivatives," *Journal of Aircraft*, Vol. 37, No. 4, 2000, pp. 676–683. doi: 10.2514/2.2651.

[11]Park, M. A. and Green, L. L., "Steady-State Computation of Constant Rotational Rate Dynamic Stability Derivatives," *AIAA-2000-4321*, 2000.

[12]Mader, C. A. and Martins, J. R. R., "Computation of Aircraft Stability Derivatives Using an Automatic Differentiation Adjoint Approach," *AIAA Journal*, Vol. 49, No. 12, December 2011, pp. 2737–2750.

[13]Widhalm, M., Hübner, A. R., and Thormann, R., "Linear Frequency Domain Predictions of Dynamic Response Data for the DLRF12 Wind Tunnel Model," *6th European Congress on Computational Methods in Applied Sciences and Engineering*, edited by J. Eberthardsteiner et al., ECCOMAS 2012, Vienna, Austria, Sept 2012.

[14]Mialon, B., Khrabrov, A., Khelil, S. B., Hübner, A., Ronch, A. D., Badcock, K., Cavagna, L., Eliasson, P., Zhang, M., Ricci, S., Jouhaud, J.-C., Rogé, G., Hitzel, S., and Lahuta, M., "Validation of numerical prediction of dynamic derivatives: The DLR-F12 and the Transcruiser test cases," *Progress in Aerospace Sciences*, Vol. 47, No. 8, 2011, pp. 674 – 694. doi: 10.1016/j.paerosci.2011.08.010.

[15]Pechloff, A. and Laschka, B., "Small Disturbance Navier-Stokes Computations Employing the Wilcox k-omega Turbulence Model," *27th Congress of the International Concil of the Aeronautical Sciences*, ICAS Paper 2010-3.10.5, Nice, France, Sept. 2010.

[16]Dufour, G., Sicot, F., Puigt, G., Liauzun, C., and Dugeai, A., "Contrasting the Harmonic Balance and Linearized Methods for Oscillating-Flap Simulations." *AIAA Journal*, Vol. 48, No. 4, 2010, pp. 788–797. doi: 10.2514/1.43401.

[17]Chassaing, J.-C. and Gerolymos, G. A., "Time-linearized time-harmonic 3-D Navier–Stokes shock-capturing schemes," *International Journal for Numerical Methods in Fluids*, Vol. 56, No. 3, 2008, pp. 279–303. doi: 10.1002/fld.1523.

[18]Pechloff, A. and Laschka, B., "Small Disturbance Navier-Stokes Computations for Low-Aspect-Ratio Wing Pitching Oscillations," *Journal of Aircraft*, Vol. 47, No. 3, 2010, pp. 737–753. doi: 10.2514/1.45233.

[19]Kim, C. S., Kim, C., and Rho, O. H., "Sensitivity Analysis for the Navier-Stokes Equations with Two-Equation Turbulence models," *AIAA Journal*, Vol. 39, No. 5, 2001, pp. 838–845. doi: 10.2514/2.1387.

[20]Thormann, R. and Widhalm, M., "Linear Frequency Domain Predictions of Dynamic Response Data for Viscous Transonic Flows," *AIAA Journal*, Vol. 51, No. 11, Oct 2013, pp. 2540–2557. doi: 10.2514/1.J051896.

[21]Saad, Y., *Iterative Methods for Sparse Linear Systems*, Society for Industrial and Applied Mathematics, 2nd ed., 2003.

[22]Campobasso, M. S. and Giles, M. B., "Effects of Flow Instabilities on the Linear Analysis of Turbomachinery Aeroelasticity," *Journal of Propulsion and Power*, Vol. 19, No. 2, 2003, pp. 250–259. doi: 10.2514/2.6106.

[23]McCracken, A. J., Ronch, A. D., Timme, S., and Badcock, K. J., "Solution of linear systems in Fourier-based methods for aircraft applications," *International Journal of Computational Fluid Dynamics*, Vol. 27, No. 2, Jan. 2013, pp. 79–87. doi: 10.1080/10618562.2012.750719.

[24]Zwaan, R. J., "LANN Wing. Pitching Oscillation," *Compendium of Unsteady Aerodynamic Measurements, Addendum No. 1*, AGARD-R-702, 1985, pp. 9–1–9–76.

[25]Spalart, P. R. and Allmaras, S. R., "A One-Equation Turbulence Model for Aerodynamic Flows," AIAA Paper 92-0439, Jan. 1992.

[26]Dwight, R. P., Brezillon, J., and Vollmer, D. B., "Efficient Algorithms for Solution of the Adjoint Compressible Navier-Stokes Equations with Applications," *7th ONERA-DLR Aerospace Symposium*, edited by ODAS, Toulouse, France, 2006, pp. 1–11.

[27]Thormann, R. and Widhalm, M., "Forced Motion Simulations using a Linear Frequency Domain Solver for a Generic Transport Aircraft," *16th International Forum of Aeroelasticity and Structural Dynamics*, IFASD 2013-017A, Bristol, UK, 2013.

[28]Saad, Y. and Schultz, M. H., "GMRES: A Generalized Minimum Residual Algorithm for Solving Nonsymmetric Linear Systems," *SIAM Journal of Scientific and Statistical Computing*, Vol. 7, No. 3, 1986, pp. 856–859. doi: 10.1137/0907058.

[29]Lindquist, D. R. and Giles, M. B., "Validity of Linearized Unsteady Euler Equations with Shock Capturing," *AIAA Journal*, Vol. 32, No. 1, 1994, pp. 46–53. doi: 10.2514/3.11949.

[30]Xu, S., Timme, S., and Badcock, K. J., "Enabling off-design linearised aerodynamics analysis using Krylov subspace recycling technique," *Computers & Fluids*, Vol. 140, 2016, pp. 385–396. doi: 10.1016/j.compfluid.2016.10.018.